# Floquet generation of a second-order topological superconductor

Arnob Kumar Ghosh [1,2,*] Tanay Nag,[3,†] and Arijit Saha [1,2,‡]
[1]*Institute of Physics, Sachivalaya Marg, Bhubaneswar-751005, India*
[2]*Homi Bhabha National Institute, Training School Complex, Anushakti Nagar, Mumbai 400094, India*
[3]*SISSA, via Bonomea 265, 34136 Trieste, Italy*

(Received 28 September 2020; revised 14 January 2021; accepted 14 January 2021; published 25 January 2021)

We theoretically investigate the Floquet generation of a second-order topological superconducting (SOTSC) phase hosting Majorana corner modes (MCMs), considering a quantum spin Hall insulator with a proximity-induced superconducting *s*-wave pairing in it. Our dynamical prescription consists of the periodic kick in time-reversal symmetry breaking the in-plane magnetic field and fourfold rotational symmetry breaking the mass term in the bulk while these Floquet MCMs are preserved by antiunitary particle-hole symmetry. The first driving protocol always leads to four zero-energy MCMs (i.e., one Majorana state per corner) as a sign of a *strong* SOTSC phase. Interestingly, the second protocol can result in a *weak* SOTSC phase, harboring eight zero-energy MCMs (two Majorana states per corner), in addition to the *strong* SOTSC phase. We characterize the topological nature of these phases by a Floquet quadrupolar moment and Floquet Wannier spectrum. We believe that relying on the recent experimental advancement in the driven systems and proximity - superconductivity, our schemes may be possible to test in the future.

DOI: 10.1103/PhysRevB.103.045424

## I. INTRODUCTION

Recently, topological superconductors (TSCs) hosting Majorana zero-energy modes at their boundaries have attracted enormous attention both theoretically and experimentally due to their connection with non-Abelian exchange statistics and potential applications in topological quantum computation [1–6]. The heterostructures of materials with strong spin-orbit coupling such as topological insulator, semiconductor thin films, and nanowires with proximity-induced superconductivity are proposed to provide an efficient platform for the realization of Majorana zero modes (MZMs) [7–11]. The latter have also been experimentally realized recently [12–16]. In such heterostructures, MZMs are usually localized at two-dimensional (2D) vortex cores or one-dimensional (1D) edges where the topological superconducting gap in the bulk spectrum changes its sign. Very recently, the conventional bulk-boundary correspondence has been generalized in the context of higher-order topological insulators (HOTIs) and higher-order topological superconductors (HOTSCs) [17–48]. Precisely, an $n$th-order topological insulator or superconductor in $m$ dimensions hosts $d_c = (m-n)$-dimensional boundary modes ($n \leqslant m$). For example, a three-dimensional (3D) second- (third-) order topological insulator (SOTI) hosts gapless modes on the hinges (corners), characterized by $d_c = 1$ (0). In particular, the SOTI phase has been experimentally realized in acoustic materials [49], photonic crystals [50,51], and electrical circuit [52] setups.

Nonequilibrium aspects of topological phases have attracted a great deal of attention in the community as the driven topological systems exhibit nontrivial properties which are absent in the corresponding static phase [53–59]. The Floquet machinery allows one to keep track of the time-dependent problem of periodically driven systems in a time-independent way with an effective Floquet Hamiltonian, defined in the frequency space [60,61]. Therefore, the equilibrium notion of the topological invariant can be extended to Floquet topological phases where anomalous edge states or Floquet Majorana modes between two consecutive Floquet Brillouin zones appear [55,62,63]. Interestingly, Floquet engineering by suitably tuning appropriate perturbation can lead to Floquet HOTI phases starting from a lower order or nontopological phases [64–77]. Therefore, a bunch of fundamentally important questions naturally arise: (a) Can the Floquet HOTSC phase be engineered by periodically driving the appropriate perturbation? (b) How does one topologically characterize the Floquet HOTSC phase? In this paper, we intend to address these intriguing questions which have not been reported so far in the literature, to the best of our knowledge.

In this paper, we demonstrate a general mechanism of engineering the Floquet SOTSC phase by periodically kicking the quantum spin Hall insulator (QSHI) Hamiltonian, proximitized by an *s*-wave superconductor. For the first case, we consider the periodic kicking in time-reversal symmetry (TRS) $\mathcal{T}$ breaking magnetic field to obtain the SOTSC phase hosting MCMs. In our second case, we introduce the kicking in fourfold rotational symmetry $C_4$ and $\mathcal{T}$ breaking terms so the underlying edge states of QSHI phases become gapped and MCMs appear due to Jackiw-Rebbi index theorem [78]. Our dynamical model is schematically illustrated in Fig. 1 where the 2D QSHI/*s*-wave superconductor heterostructure is depicted with the general dynamical kicking protocol of perturbation $V(t)$. The MCMs appear between adjacent boundaries (edges I, II, III, and IV). We analytically

*arnob@iopb.res.in
†tnag@sissa.it
‡arijit@iopb.res.in

 

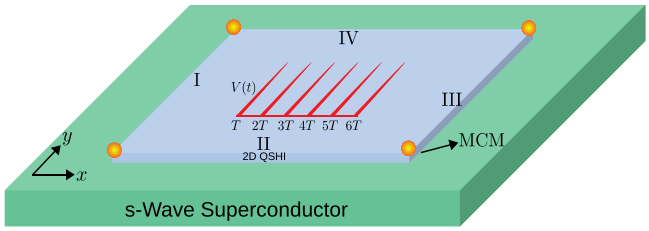


FIG. 1. Schematic of our setup is illustrated in presence of periodic kick (red, grey) as an external drive. Here, a 2D QSHI (violet, light grey) is placed in close proximity to a bulk $s$-wave superconductor (green, grey). MCMs are shown by circular dots (orange, light grey) and the four edges of the 2D QSHI are denoted by I, II, III, IV.

derive the effective edge Hamiltonian for both the driven cases mentioned above to analyze the domain-wall formation associated with the sign change of Dirac mass of the underlying low-energy Hamiltonian. These SOTSC phases are appropriately characterized by both Floquet Wannier spectra (FWS) and Floquet quadrupolar moments (FQMs).

The remainder of the paper is organized as follows. In Sec. II, we introduce our model Hamiltonian and the driving protocol. In Sec. III, we provide the effective Floquet Hamiltonian and illustrate the emergence of Floquet MCMs in the local density of states (LDOS) behavior. In Sec. IV, we characterize the higher order topological phase hosting MCMs by employing the appropriate topological invariants FQMs and FWS that are extensively discussed in Appendix A. In Sec. V, we resort to low-energy edge theory to understand the analytical solutions of the zero-energy MCMs. We provide the detailed analysis of that in Appendixes B and C. In Sec. VI, we provide our alternative dynamical protocol to realize the MCMs, and the necessary calculational details are properly supplemented in Appendixes B and C. Finally, in Sec. VII, we summarize and conclude our results.

## II. MODEL HAMILTONIAN AND DRIVING PROTOCOL

We begin with the static Hamiltonian of a 2D QSHI placed in close proximity to a bulk $s$-wave superconductor [39],

$$H_0 = \mathbf{N}(k)\cdot\mathbf{\Gamma}\,, \tag{1}$$

with $\mathbf{N}(k) = (N_1(k), N_2(k), N_3(k), N_4)$, $N_1(k) = 2\lambda_x \sin k_x$, $N_2(k) = 2\lambda_y \sin k_y$, $N_3(k) = \xi_k = (m_0 - 2t_x\cos k_x - 2t_y \cos k_y)$, and $N_4 = \Delta$. Here, $t_{x,y}$ and $\lambda_{x,y}$ represent the nearest-neighbor hopping and spin-orbit coupling, respectively, $\Delta$ is the superconducting gap induced via the proximity effect, $m_0$ is the crystal-field splitting energy, and $\mu$ is the chemical potential. Also, $\Gamma_1 = \sigma_x s_z$, $\Gamma_2 = \sigma_y\tau_z$, $\Gamma_3 = \sigma_z\tau_z$, and $\Gamma_4 = s_y\tau_y$. The three Pauli matrices $\boldsymbol{\sigma}$, $\boldsymbol{s}$, and $\boldsymbol{\tau}$ act on orbital $(a, b)$, spin $(\uparrow, \downarrow)$, and particle-hole degrees of freedom, respectively. We work in the following basis: $C_k = (c_{k,a\uparrow}, c^\dagger_{-k,a\uparrow}, c_{k,a\downarrow}, c^\dagger_{-k,a\downarrow}, c_{k,b\uparrow}, c^\dagger_{-k,b\uparrow}, c_{k,b\downarrow}, c^\dagger_{-k,b\downarrow})^T$. We consider chemical potential $\mu = 0$ to obtain analytical results for the edge modes, otherwise, $\mu\tau_z$ can be added to the Hamiltonian [Eq. (1)].

The Hamiltonian represented by Eq. (1) preserves TRS $\mathcal{T} = is_yK$ with $K$ being the complex conjugation. If $\Delta = 0$, the QSHI phase is observed when $[m_0^2 - (2t_x + 2t_y)^2][m_0^2 - (2t_x - 2t_y)^2] < 0$ [79], hosting gapless propagating helical edge modes [80–82]. When $\Delta \neq 0$, a superconducting gap opens both in the bulk and helical edge spectrum and the system becomes a trivial BCS superconductor [39]. Interestingly, Hamiltonian [Eq. (1)] continues satisfying the unitary chiral symmetry $\mathcal{P} = \sigma_x s_y \tau_z$ and antiunitary particle-hole symmetry $\mathcal{C} = \tau_x K$. These two symmetries turn out to be very important in determining the robustness of the SOTSC phase.

We now introduce our driving protocol in the form of periodic kick as follows:

$$V(t) = h_x\Gamma_5 \sum_{r=1}^{\infty}\delta(t - rT) \tag{2}$$

and

$$V(t) = \Lambda(k)\Gamma_6 \sum_{r=1}^{\infty}\delta(t - rT)\,, \tag{3}$$

where, Eq. (2) represents the TRS breaking driving protocol due to the in-plane Zeeman field $h_x$ applied along $x$ direction, $T$ is the period of the drive, $\Gamma_5 = s_x\tau_z$, and $\Gamma_6 = \sigma_x s_x \tau_z$. Here, the physical meaning of $\Gamma_6$ can be understood in terms of some hopping parameter that simultaneously flips both the orbital and spin. The detailed outcome of $C_4$ and TRS symmetry breaking driving protocol [Eq. (3)] will be discussed in Sec VI. In the static limit, $H^1_{\rm sta} = H_0 + h_x\Gamma_5$, is found to host MCMs in the SOTSC phase when $h_x > \Delta$ [39]. The quasiparticle band gap of the edges does not close along $k_y$ direction while the gap can be tuned along the $k_x$ direction, resulting in a topological phase transition and exponentially localized MCMs appear at zero energy protected by $\mathcal{P}$ and $\mathcal{C}$ symmetries, although the bulk always remains gapped.

## III. EFFECTIVE FLOQUET HAMILTONIAN

Following the periodic kick [see Eq. (2)], the Floquet operator reads

$$\begin{aligned} U(T) &= \widetilde{\mathcal{T}\mathcal{O}}\exp\left[-i\int_0^T dt(H_0 + V(t))\right] \\ &= \exp(-iH_0T)\,\exp(-ih_x\Gamma_5)\,. \end{aligned} \tag{4}$$

We can write $U(T)$ in a more compact form as

$$U(T) = C_T(n_0 - in_5\Gamma_5) - iS_T\sum_{j=1}^{4}(m_j\Gamma_j + p_j\Gamma_{j5})\,, \tag{5}$$

where, $C_T = \cos(|\mathbf{N}(k)|T)$, $S_T = \sin(|\mathbf{N}(k)|T)$, $n_0 = \cos h_x$, $n_5 = \sin h_x$, $m_j = \frac{N_j(k)\cos h_x}{|\mathbf{N}(k)|}$, $p_j = \frac{N_j(k)\sin h_x}{|\mathbf{N}(k)|}$, and $\Gamma_{j5} = \frac{1}{2i}[\Gamma_j, \Gamma_5]$ with $j = 1, 2, 3, 4$. The general form of the effective Hamiltonian is thus found to be

$$H^I_{\rm eff} = \frac{\epsilon_k}{\sin\epsilon_k T}\left[\sin(|\mathbf{N}(k)|T)\cos h_x\sum_{j=1}^{4}n_j\Gamma_j + \cos(|\mathbf{N}(k)|T)\sin h_x\Gamma_5 + \sin(|\mathbf{N}(k)|T)\sin h_x\sum_{j=1}^{4}n_j\Gamma_{j5}\right], \tag{6}$$

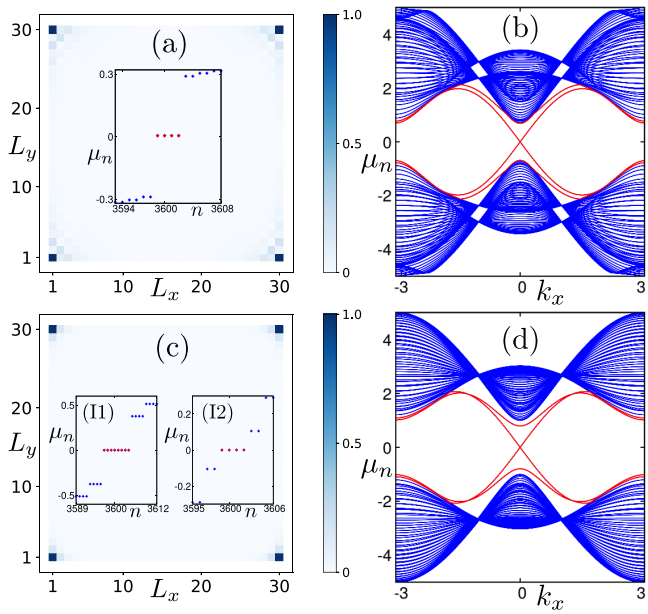


FIG. 2. (a) LDOS in finite geometry is demonstrated for driving protocol [Eq. (2)] and inset exhibits the eigenvalue spectrum for the same. Here, $L_x = L_y = 30, m_0 = t_x = t_y = \lambda_x = \lambda_y = 1.0$, $\Delta = 0.4, h_x = 0.4, T = 0.628$. (b) The edge spectrum is shown for open boundary condition along $y$ direction for Eq. (7). The edge gap closes when $\Delta = \frac{h_x}{T}$. (c) LDOS in finite geometry and eigenvalue spectrum [insets (I1) and (I2)] are depicted for driving protocol [Eq. (3)]. We choose $\Lambda = 0.3$ and the value of the other parameters remain the same as panel (a). For insets (I1) and (I2), we choose the parameter regime as $|\frac{m\Lambda}{2t_xT}|, |\frac{m\Lambda}{2t_yT}| > \Delta$, and $|\frac{m\Lambda}{2t_xT}| < \Delta < |\frac{m\Lambda}{2t_yT}|$, respectively. (d) The edge spectrum is shown for open boundary condition along $y$ direction for the effective Hamiltonian [Eq. (11)]. The edge gap closes when $\Delta = |\frac{m\Lambda}{2t_xT}|$. See text for discussion.

with $\epsilon_k = \frac{1}{T}\cos^{-1}[\cos(|\mathbf{N}(k)|T)\cos h_x]$, $n_j = \frac{N_j(k)}{|\mathbf{N}(k)|}$. In the high-frequency limit i.e., $T \to 0$ and $h_x \to 0$, neglecting the higher-order terms in $T$ and $h_x$, we find

$$H^I_{\rm eff} \approx \sum_{j=1}^{4} N_j(k)\Gamma_j + \frac{h_x}{T}\Gamma_5 + h_x \sum_{j=1}^{4} N_j(k)\Gamma_{j5} \,. \qquad (7)$$

Note that in Eq. (7), terms associated with $\Gamma_{j5}$ appears due to the drive and are absent in the static model; interestingly, only $\Gamma_{15}$ among $\Gamma_{j5}$ does not commute with $H^I_{\rm sta}$. As a result, $H^I_{\rm eff}$ loses the chiral symmetry generated by the unitary operator $\mathcal{P}$. Remarkably, $H^I_{\rm eff}$ preserves the particle-hole symmetry, which allows the generation of a Floquet SOTSC phase with MCMs after the dynamical breaking of TRS. We now tie up our analytical finding by numerically diagonalizing the exact Floquet operator [Eq. (4)] in the open boundary condition (OBC). One can obtain Floquet quasistates $|\phi_n\rangle$ and quasienergies $\mu_n$ from $U(T)$: $U(T)|\phi_n\rangle = \exp(-i\mu_n T)|\phi_n\rangle$. We present the LDOS associated with the zero (within numerical accuracy) quasienergy Floquet quasistates in Fig. 2(a). These zero-energy quasistates correspond to the MCMs which are localized at the four corners of the system.

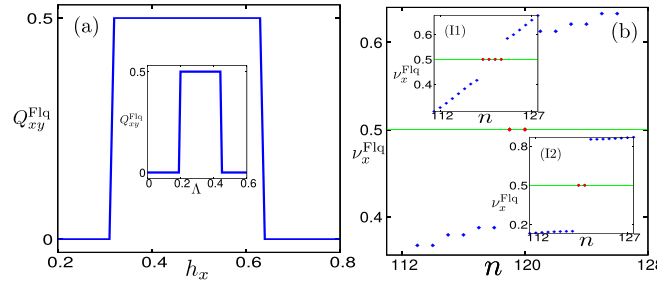


FIG. 3. (a) Variation of FQM $Q^{\rm Flq}_{xy}$ is demonstrated as a function $h_x$ for driving protocol [Eq. (2)]. In the inset, the same has been depicted with respect to $\Lambda$ for driving protocol [Eq. (3)]. We choose $L_x = L_y = 16, m_0 = t_x = t_y = \lambda_x = \lambda_y = 1.0$, $\Delta = 0.4, T = 0.628$. (b) FWS $\nu^{\rm Flq}_x$ with respect to the state index is shown for driving protocol Eqs. (2) and (3), insets (I1) and (I2) respectively. For driving protocol [Eq. (2)], we choose $h_x > \Delta T$. Insets (I1) and (I2) have been depicted for the parameter regime $|\frac{m\Lambda}{2t_xT}|, |\frac{m\Lambda}{2t_yT}| > \Delta$, and $|\frac{m\Lambda}{2t_xT}| < \Delta < |\frac{m\Lambda}{2t_yT}|$, respectively, for driving protocol [Eq. (3)].

## IV. TOPOLOGICAL CHARACTERIZATION OF MCMS

To analyze the topological robustness of the Floquet MCMs in the SOTSC phase, we numerically compute the FQM [based on Floquet quasistates obtained from numerical diagonalization of Eq. (4)], $Q^{\rm Flq}_{xy}$, and the FWS $\nu^{\rm Flq}_x$ [based on $T \to 0$ effective Hamiltonian Eq. (7)] as shown in Figs. 3(a) and 3(b), respectively. At the outset, we note that in the static limit, these invariants possess a quantized value of 0.5. The FQM is defined through the Floquet many-body ground state $n_F$ composed by arranging the occupied quasistates columnwise associated with the quasienergy $-\omega/2 \leqslant \mu_n \leqslant 0$: $n_F = \sum_{n\in\mu_n\leqslant 0} |\phi_n\rangle\langle\phi_n|$ [64,69]. We obtain $Q^{\rm Flq}_{xy} \equiv \mathrm{mod}(Q^{\rm Flq}_{xy}, 1) = 0.5$, this quantization [for a finite range of $h_x$ in protocol [Eq. (2)] is depicted in Fig. 3(a) and clearly suggests that the SOTSC phase, hosting MCMs, is topologically robust. Furthermore, we compute another invariant, namely, the eigenvalue $\nu^{\rm Flq}_x$ of Floquet Wannier Hamiltonian $\mathcal{H}^{\rm Flq}_{\mathcal{W}_x}$. The FWS $\nu^{\rm Flq}_x$ ($\nu^{\rm Flq}_y$), demonstrated in Fig. 3(b), exhibits two isolated eigenvalues at 0.5, referring to the signature of MCMs in the SOTSC phase for this protocol. We refer the readers to Appendix A for the detailed calculation of FWS $\nu^{\rm Flq}_x$ ($\nu^{\rm Flq}_y$).

## V. LOW-ENERGY EDGE THEORY

Here we proceed to derive the edge theory for the Floquet case starting from the effective Hamiltonian [Eq. (7)] in $T \to 0$ limit. The low-energy effective Hamiltonian around $\Gamma = (0, 0)$ point can be written as

$$H^{\rm I}_{\rm eff,k} \approx \big(m + t_x k_x^2 + t_y k_y^2\big)\Gamma_3 + 2\lambda_x k_x \Gamma_1 + 2\lambda_y k_y \Gamma_2 + \Delta\Gamma_4 + \frac{h_x}{T}\Gamma_5 + 2\lambda_x h_x k_x \Gamma_{15} \,, \qquad (8)$$

where $m = (m_0 - 2t_x - 2t_y)$ and we assume $m < 0$ to satisfy the topological condition [79]. We consider here the minimal model as $\Gamma_{15}$ is only incorporated among all the $\Gamma_{j5}$. As a representative example, for edge I, we employ OBCs [periodic boundary conditions (PBCs)] along the $x$ ($y$) direction.

One can thus rewrite $H^{I}_{\text{eff,k}} = H_I(-i\partial_x) + H_P(-i\partial_x, k_y, h_x)$, neglecting the $k_y^2$ term. Here, $H_I = (m - t_x\partial_x^2)\Gamma_3 - 2i\lambda_x\partial_x\Gamma_1$ and $H_P = 2\lambda_y k_y\Gamma_2 + \Delta\Gamma_4 + \frac{h_x}{T}\Gamma_5 - 2i\lambda_x h_x\partial_x\Gamma_{15}$. Assuming $\Psi$ to be the zero-energy eigenstate of $H_I$, we obtain (see Appendix B for details)

$$\Psi_\alpha = |\mathcal{N}_x|^2 e^{-\mathcal{A}x}\sin\mathcal{B}x e^{ik_y y}\Phi_\alpha\ , \tag{9}$$

where $\mathcal{A} = \frac{\lambda_x}{t_x}$, $\mathcal{B} = \sqrt{|\frac{m}{t_x}| - \mathcal{A}^2}$, $|\mathcal{N}_x|^2 = \frac{4\mathcal{A}(\mathcal{A}^2+\mathcal{B}^2)}{\mathcal{B}^2}$ and $\Phi_\alpha$ is an eight-component spinor satisfying $\sigma_y s_z\tau_z\Phi_\alpha = -\Phi_\alpha$. We choose the following basis: $\Phi_1 = |\sigma_y = +1\rangle \otimes |s_z = +1\rangle \otimes |\tau_z = -1\rangle$, $\Phi_2 = |\sigma_y = -1\rangle \otimes |s_z = +1\rangle \otimes |\tau_z = +1\rangle$, $\Phi_3 = |\sigma_y = -1\rangle \otimes |s_z = -1\rangle \otimes |\tau_z = -1\rangle$, $\Phi_4 = |\sigma_y = +1\rangle \otimes |s_z = -1\rangle \otimes |\tau_z = +1\rangle$ to cast the effective Hamiltonian for edge I as $H_i^{\text{I,edge}} = -2\lambda_y k_y s_z - \Delta s_y\tau_y$. Now the low-energy effective Hamiltonian for the $l$th edge is given as (see Appendix B for details)

$$H_l^{\text{I,edge}} = -iA_l s_z\partial_l - iB_l s_y\tau_z\partial_l - \Delta s_y\tau_y - h_l s_x\tau_z\ , \tag{10}$$

with $A_l = \{-2\lambda_y, 2\lambda_x, -2\lambda_y, 2\lambda_x\}$, $B_l = \{0, -2\lambda_x h_x, 0, -2\lambda_x h_x\}$, and $h_l = \{0, \frac{h_x}{T}, 0, \frac{h_x}{T}\}$. One can thus observe that the superconducting pairing gap has been induced in all the helical edge states irrespective of the Zeeman fields in that edge as $\{s_z, s_y\tau_y\} = 0$. On the other hand, $h_x$ can only open up a Zeeman gap on two parallel edges (II and IV) without affecting two other perpendicular edges (I and III). We depict the quasienergy spectrum of the semi-infinite slab geometry in Fig. 2(b) to manifest the gap closing at $\Delta = \frac{h_x}{T}$.

In $\tau_x = \pm s_z$ subspace, the last term in Eq. (10) can be written as $h_l s_x\tau_z \to \mp h_l s_y\tau_y$. We eventually obtain two decoupled diagonal blocks with Dirac masses $\Delta \pm \frac{h_x}{T}$ for edge II while, for edge I, the Dirac masses are of the same sign in these blocks. Therefore, for $h_x > \Delta T$, Dirac masses on edges I and II carry opposite signs, leading to localized MCMs at the intersection of two perpendicular edges. Interestingly, compared to the static case, the MCMs in the Floquet SOTSC phase can be observed for a much smaller value of the in-plane magnetic field $h_x$ as $T \to 0$ in the high-frequency limit. One can find the wave function for the zero-energy MCM localized at the intersection between edges I and II, as $\Psi_C \sim \exp[-(\Delta/2\lambda_y)y]\Phi_C$ and $\Psi_C \sim \exp[-(|h_x - \Delta T|/2\lambda_x T)x]\Phi_C$ for edges I and II, respectively, with $\Phi_C = \{1, -1, i, i\}^T$ (see Appendix C for the derivation). The localization length of MCM can be different in different directions when $|h_x - \Delta T|/2\lambda_x T \neq \Delta/2\lambda_y$ and it can be controlled along edge II by the period or frequency of the Floquet driving.

## VI. ALTERNATIVE DYNAMICAL PROTOCOL FOR REALIZING MCMS

Having established a route to obtain Floquet SOTSC starting from a static proximity-induced QSHI, we here demonstrate another driving protocol to obtain the same by breaking the $C_4$ symmetry and TRS of the QSHI phase instead of an in-plane Zeeman field discussed before. We work with the dynamical protocol given in Eq. (3), where $\Lambda(k) = \Lambda(\cos k_x - \cos k_y)$. Upon adding this term with the static Hamiltonian [Eq. (1)], $H^{\text{II}}_{\text{sta}} = H_0 + \Lambda(k)\Gamma_6$, one can find MCMs localized at zero energy and protected by unitary $\mathcal{P}$ and antiunitary $\mathcal{C}$ symmetry [38]. Following our dynamical protocol, we numerically diagonalize the Floquet operator [Eq. (4)] for this case and find strong corner localization of Majorana modes. In this case, eight Floquet MCMs appear at quasienergy $\mu_n = 0$ (within numerical accuracy) as shown in Fig. 2(c)(I1). The MCMs obtained here are characteristically different from that originated by kicking the in-plane magnetic field where four zero-energy MCMs are observed. For $h_x$ kicking [Eq. (2)], the individual single-particle state residing at $\mu_n = 0$ exhibits Majorana localization at a single corner. On the other hand, for $\Lambda(k)$ kicking [Eq. (3)], we find there exist at least two single-particle states sharing individual corners.

For this protocol also, we derive the Floquet operator as follows: $U(T) = C_T(n_0 - in_6\Gamma_6) - iS_T\sum_{j=1}^4(m_j\Gamma_j + p_j\Gamma_{j6})$ where, $C_T = \cos(|\mathbf{N}(k)|T)$, $S_T = \sin(|\mathbf{N}(k)|T)$, $n_0 = \cos\Lambda(k)$, $n_6 = \sin\Lambda(k)$, $m_j = \frac{N_j(k)\cos\Lambda(k)}{|\mathbf{N}(k)|}$, $p_j = \frac{N_j(k)\sin\Lambda(k)}{|\mathbf{N}(k)|}$ and $\Gamma_{j6} = \frac{1}{2i}[\Gamma_j, \Gamma_6]$. In the high-frequency limit $T \to 0$ and $\Lambda \to 0$, the effective Floquet Hamiltonian takes the form

$$H^{II}_{\text{eff}} \approx \sum_{j=1}^4 N_j(k)\Gamma_j + \frac{\Lambda(k)}{T}\Gamma_6 + \Lambda(k)\sum_{j=1}^4 N_j(k)\Gamma_{j6}\ . \tag{11}$$

Similar to the effective Hamiltonian [Eq. (7)], here the drive-induced terms are associated with $\Gamma_{j6}$, which essentially break the unitary symmetry $\mathcal{P}$. Importantly, the antiunitary particle-hole symmetry generated by $\mathcal{C}$ assure the zero-energy states are localized at the corners. Following the same procedure described for the previous protocol, we obtain the low-energy effective Hamiltonian of the edges in the edge-coordinate $l$ as (see Appendix B for details)

$$H_l^{\text{II,edge}} = -iA_l s_z\partial_l + iB_l s_x\partial_l - \Delta s_y\tau_y + \Lambda_l s_y\ , \tag{12}$$

with $A_l = \{-2\lambda_y, 2\lambda_x, -2\lambda_y, 2\lambda_x\}$, $B_l = \{\frac{m\lambda_y\Lambda}{t_x}, \frac{m\lambda_x\Lambda}{t_y}, \frac{m\lambda_y\Lambda}{t_x}, \frac{m\lambda_x\Lambda}{t_y}\}$ and $\Lambda_l = \{-\frac{m\Lambda}{2t_xT}, \frac{m\Lambda}{2t_yT}, -\frac{m\Lambda}{2t_xT}, \frac{m\Lambda}{2t_yT}\}$. For more insight, let us first consider $\Delta = 0$. It is evident that $\Lambda_l$ changes signs at each corner and leads to a domain-wall formation of Dirac mass causing zero-energy Jackiw-Rebbi modes to appear at the corners [64,69,78]. Due to the inclusion of the superconducting correlation, $H_l^{\text{II,edge}}$ can be decomposed into two independent parts as

$$H_l^{\text{II,edge}} = H_{\tau_y=+1} \oplus H_{\tau_y=-1}\ , \tag{13}$$

where

$$\begin{aligned} H_{\tau_y=+1} &= -iA_l s_z\partial_l + iB_l s_x\partial_l + [-\Delta + \Lambda_l]s_y, \\ H_{\tau_y=-1} &= -iA_l s_z\partial_l + iB_l s_x\partial_l + [\Delta + \Lambda_l]s_y\ . \end{aligned} \tag{14}$$

The domain walls for both sectors $\tau_y = \pm 1$ appear when $|\frac{m\Lambda}{2t_xT}|, |\frac{m\Lambda}{2t_yT}| > \Delta$. As a result, one finds two MCMs solutions [see Fig. 2(c)(I1)] per corner with the superposed wave function $\Psi_C \sim \alpha\ e^{-\frac{M_1-\Delta}{2\lambda_y}y}\Phi_C^1 + \beta\ e^{-\frac{M_1+\Delta}{2\lambda_y}y}\Phi_C^2$ for edge I. This phenomenon does not appear in the $h_x$-kick case where the domain wall for the Dirac mass appears only in one block of the edge Hamiltonian and the other block remains inactive (massive). On the other hand, for $|\frac{m\Lambda}{2t_xT}| < \Delta < |\frac{m\Lambda}{2t_yT}|$, the domain walls exist in $\tau_y = +1$ block, but not in $\tau_y = -1$ block. This results in a situation where only one MCM can present at

each corner [see Fig. 2(c)(I2)] with the wave function $\Psi_C \sim e^{-\frac{M_I+\Delta}{2\lambda_y}y}\Phi_C^1$ for edge I. See Appendix C for the derivation of the MCMs wave functions. The gap closing at $\Delta = |\frac{m\Lambda}{2t_xT}|$ has been illustrated in Fig. 2(d) based on a slab geometry calculation.

We also calculate the FQM which appears to be $Q_{xy}^{\rm Flq} = 0.0\,(0.5)$ [see inset of Fig. 3(a)] when there exist eight (four) MCMs at zero energy [see Figs. 2(c)(I1) and 2(c)(I2)]. This is because two MCMs sharing each corner can fuse to a fermionic mode, resulting in vanishing $Q_{xy}^{\rm Flq}$. On the other hand, one can find four (two) $\nu_{x(y)}^{\rm Flq} = 0.5$ eigenvalues associated with the Floquet Wannier Hamiltonian for the SOTSC phase with eight (four) zero-energy MCMs as shown in Figs. 3(b)(I1) and (3(b)(I2). While for $h_x$ kick, there exist only two $\nu_x^{\rm Flq} = 0.5$ eigenvalues associated with four zero-energy MCMs. Thus one can infer that eight (four) MCMs represent the *weak (strong)* SOTSC phase. However, this subtlety cannot be distinguished from the feature of LDOS [see Figs. 2(a) and 2(c)].

## VII. SUMMARY AND CONCLUSIONS

To summarize, in this paper, we demonstrate two dynamical protocols to generate Floquet SOTSC phases hosting MCMs. In particular, a kick in the in-plane Zeeman field $h_x$, breaking the TRS, can lead to a *strong* SOTSC phase hosting only one MCM at each corner. In comparison, a $C_4$ and TRS breaking perturbation $\Lambda(k)$ can lead to eight (four) MCMs referring to *weak (strong)* SOTSC phase. We investigate the emergence of dynamical MCMs, localized at zero quasienergy, by numerically diagonalizing the exact Floquet operator and analytically from the effective edge Hamiltonian. We show that these MCMs are protected by the antiunitary particle-hole symmetry. We also characterize these phases by appropriate topological invariants such as FQM ($Q_{xy}^{\rm Flq}$) and FWS [$\nu_x^{\rm Flq}$ ($\nu_y^{\rm Flq}$)].

As far as the experimental feasibility of our setup is concened, superconductivity in QSHIs can be induced via proximity effect (e.g., $NbSe_2$) [83,84] with an induced gap $\Delta \sim 0.7$ meV [84]. In recent times, experimental advancements on pump-probe techniques [58,85,86] have enabled one to observe Floquet topological insulators [85]. Therefore, we believe that the signature of MCMs may be possible to achieve via pump-probe-based local scanning tunneling microscope (STM) measurements [87] for an in-plane magnetic field $h_x \sim 7 - 8$ T. On the other hand, our alternative dynamical protocol for generating SOTSC phases can in principle be realized in optical lattice platforms where spin-orbit coupling, flipping the spin, is theoretically proposed [88–92] and experimentally realized [90,93–96]. Moreover, the synthetic spin-orbit coupling can in principle be realized in acoustic material [97]. In recent times, Floquet driving has been experimentally demonstrated in various meta-materials such as piezoelectric material [98], acoustic systems [86], and photonic systems [57], etc. In particular, anomalous Floquet topological insulator (AFTI) has been experimentally demonstrated in acoustic systems [86]. The model of AFTIs is a 2D coupled metamaterial ring lattice. One can introduce an orbital-like degree of freedom ($\boldsymbol{\sigma}$) to the rings with two artificial atoms (ring resonators) $A$ and $B$ [99]. Also one can define a pseudospin ($\boldsymbol{s}$) for acoustic waves based on wave circulation direction in each ring within the lattice. Thus, introducing the ring pseudospin degree of freedom and the proper inter-ring coupling, a synthetic spin-orbit interaction can be successfully induced which breaks the pseudospin conservation [97]. Therefore, an acoustic wave carrying a pseudospin in one lattice ring may tunnel into the adjacent coupled ring with the pseudospin flipped and in that process both orbital and spin can be effectively flipped. Hence, our alternative dynamical protocol [Eq. (3)] is pertinent as far as the experiments on optical lattices and acoustic systems are concerned.

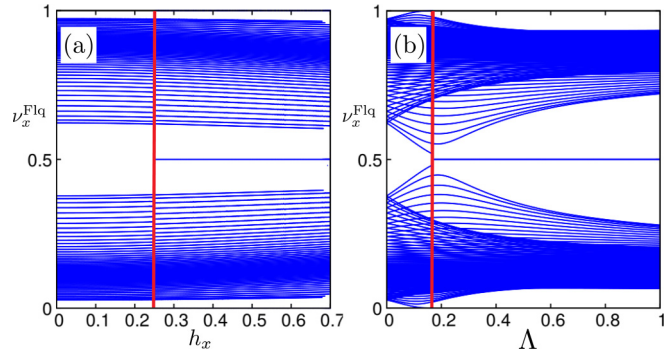


FIG. 4. (a) FWS is shown as a function of the in-plane magnetic field $h_x$ for driving protocol 1 [Eq. (2) in the main text]. (b) FWS is illustrated as a function of the $C_4$ and $\mathcal{T}$ breaking mass term $\Lambda$ for driving protocol 2 [Eq. (3) in the main text].


## ACKNOWLEDGMENT

We acknowledge SAMKHYA: High-Performance Computing Facility at Institute of Physics, Bhubaneswar, for our numerical computations.


## APPENDIX A: FLOQUET WANNIER SPECTRA

In the semi-infinite geometry (considering PBCs and OBCs along $x$ and $y$ directions, respectively), we construct the Wilson loop operator [19] $\mathcal{W}_x = F_{x,k_x+(N_x-1)\Delta k_x}\cdots F_{x,k_x+\Delta k_x}F_{x,k_x}$ with $[F_{x,k_x}]_{mn} = \langle\phi_{n,k_x+\Delta k_x}|\phi_{m,k_x}\rangle$, where $\Delta k_x = 2\pi/N_x$ ($N_x$ being the number of discrete points considered inside the Brillouin zone along $k_x$) and $|\phi_{m,k_x}\rangle$ is the $m$th occupied Floquet quasistate. The latter can be obtained by diagonalizing the effective Floquet Hamiltonian in the high-frequency limit. One can thus obtain the Wannier Hamiltonian, $\mathcal{H}_{\mathcal{W}_x}^{\rm Flq} = -i\ln\mathcal{W}_x$, whose eigenvalues $2\pi\nu_x^{\rm Flq}$ correspond to the FWS. Here, $\nu_x^{\rm Flq} \equiv {\rm mod}(\nu_x^{\rm Flq}, 1)$ is the Wannier center. One can similarly find $\nu_y^{\rm Flq}$. The feature of FWS characterizes the topological phase transition from a trivial to HOTSC phase in our case. In the Floquet HOTSC phase, it acquires a quantized value 0.5 as shown in Fig. 4.

## APPENDIX B: LOW-ENERGY EDGE THEORY

Here, we present the details of the low-energy edge theory calculation for both our driving protocols.

### 1. Driving by in-plane magnetic field $h_x$

We begin by writing down the low-energy effective Hamiltonian in the high-frequency limit [Eq. (7) in the main text] around the $\Gamma = (0, 0)$ point,

$$H^I_{\text{eff,k}} \approx \big(m + t_x k_x^2 + t_y k_y^2\big)\Gamma_3 + 2\lambda_x k_x \Gamma_1 + 2\lambda_y k_y \Gamma_2 + \Delta\Gamma_4 + \frac{h_x}{T}\Gamma_5 + 2\lambda_x h_x k_x \Gamma_{15} \,, \tag{B1}$$

For edge II, we consider PBCs (OBCs) along $x$ ($y$) direction. Hence, we replace $k_y$ by $-i\partial_y$ and rewrite $H^I_{\text{eff,k}} = H_I(-i\partial_y) + H_P(-i\partial_y, k_x, h_x)$, neglecting $k_x^2$ term with

$$H_I = \big(m - t_y \partial_y^2\big)\Gamma_3 - 2i\lambda_y \partial_y \Gamma_2 \,,$$
$$H_P = 2\lambda_x k_x \Gamma_1 + \Delta\Gamma_4 + \frac{h_x}{T}\Gamma_5 + 2\lambda_x h_x k_x \Gamma_{15} \,. \tag{B2}$$

Here, we choose $m < 0$ to satisfy the Fu-Kane criteria [79]. We solve $H_I$ exactly and treat $H_P$ as a perturbation. This approximation is valid when we assume the pairing amplitude, $\Delta$, and the amplitude of the in-plane magnectic field, $h_x$ to be small [39]. We also consider any term multiplied by $h_x$ or $\Delta$ to be small.

Assuming $\Psi$ to be the zero-energy eigenstate of $H_I$, following the boundary condition $\Psi(0) = \Psi(\infty) = 0$, we obtain

$$\Psi_\alpha = |\mathcal{N}_y|^2 e^{-\tilde{\mathcal{A}}y} \sin\tilde{\mathcal{B}}y \; e^{ik_x x}\chi_\alpha \,, \tag{B3}$$

where $\tilde{\mathcal{A}} = \frac{\lambda_y}{t_y}$, $\tilde{\mathcal{B}} = \sqrt{|\frac{m}{t_y}| - \tilde{\mathcal{A}}^2}$, $|\mathcal{N}_y|^2 = \frac{4\tilde{\mathcal{A}}(\tilde{\mathcal{A}}^2+\tilde{\mathcal{B}}^2)}{\tilde{\mathcal{B}}^2}$ and $\chi_\alpha$ is an eight-component spinor satisfying $\sigma_x\chi_\alpha = \chi_\alpha$. We work in the following basis for $\chi_\alpha$ as

$$\chi_1 = |\sigma_x = +1\rangle \otimes |s_z = +1\rangle \otimes |\tau_z = -1\rangle \,,$$
$$\chi_2 = |\sigma_x = +1\rangle \otimes |s_z = +1\rangle \otimes |\tau_z = +1\rangle \,,$$
$$\chi_3 = |\sigma_x = +1\rangle \otimes |s_z = -1\rangle \otimes |\tau_z = -1\rangle \,,$$
$$\chi_4 = |\sigma_x = +1\rangle \otimes |s_z = -1\rangle \otimes |\tau_z = +1\rangle \,. \tag{B4}$$

The matrix element of $H_P$ in this basis reads

$$H^{\text{I,edge}}_{ii,\alpha\beta} = \int_0^\infty dy \; \Psi^\dagger_\alpha(y) H_P(-i\partial_y, k_x, h_x)\Psi_\beta(y) \,. \tag{B5}$$

Thus we obtain the effective Hamiltonian for edge II as

$$H^{\text{I,edge}}_{ii} = 2\lambda_x k_x s_z - 2\lambda_x h_x k_x s_y \tau_z - \Delta s_y \tau_y - \frac{h_x}{T} s_x \tau_z \,, \tag{B6}$$

Similarly, for edge IV, we obtain the effective Hamiltonian as

$$H^{\text{I,edge}}_{iv} = 2\lambda_x k_x s_z - 2\lambda_x h_x k_x s_y \tau_z - \Delta s_y \tau_y - \frac{h_x}{T} s_x \tau_z \,. \tag{B7}$$

For edge III, we consider OBCs (PBCs) along $x$ ($y$) direction. One can thus rewrite $H^{\text{I}}_{\text{eff,k}} = H_I(-i\partial_x) + H_P(-i\partial_x, k_y, h_x)$ by replacing $k_x \to -i\partial_x$ and neglecting the $k_y^2$ term with

$$H_I = \big(m - t_x \partial_x^2\big)\Gamma_3 - 2i\lambda_x \partial_x \Gamma_1 \,,$$
$$H_P = 2\lambda_y k_y \Gamma_2 + \Delta\Gamma_4 + \frac{h_x}{T}\Gamma_5 - 2i\lambda_x h_x \partial_x \Gamma_{15} \,. \tag{B8}$$

Assuming $\Psi$ to be the zero-energy eigenstate of $H_I$, following the boundary condition $\Psi(0) = \Psi(-\infty) = 0$, and proceeding in a similar manner as before, we obtain

$$\Psi_\alpha = |\mathcal{N}_x|^2 e^{\mathcal{A}x} \sin\mathcal{B}x \; e^{ik_y y}\Phi'_\alpha \,, \tag{B9}$$

where $\mathcal{A} = \frac{\lambda_x}{t_x}$, $\mathcal{B} = \sqrt{|\frac{m}{t_x}| - \mathcal{A}^2}$, $|\mathcal{N}_x|^2 = \frac{4\mathcal{A}(\mathcal{A}^2+\mathcal{B}^2)}{\mathcal{B}^2}$ and $\Phi'_\alpha$ is an eight-component spinor satisfying $\sigma_y s_z \tau_z \Phi'_\alpha = \Phi'_\alpha$. We choose the following basis:

$$\Phi'_1 = |\sigma_y = -1\rangle \otimes |s_z = -1\rangle \otimes |\tau_z = +1\rangle \,,$$
$$\Phi'_2 = |\sigma_y = +1\rangle \otimes |s_z = -1\rangle \otimes |\tau_z = -1\rangle \,,$$
$$\Phi'_3 = |\sigma_y = +1\rangle \otimes |s_z = +1\rangle \otimes |\tau_z = +1\rangle \,,$$
$$\Phi'_4 = |\sigma_y = -1\rangle \otimes |s_z = +1\rangle \otimes |\tau_z = -1\rangle \,. \tag{B10}$$

The matrix element of $H_P$ in this basis can be written as

$$H^{\text{I,edge}}_{iii,\alpha\beta} = \int_{-\infty}^0 dx \; \Psi^\dagger_\alpha(x) H_P(-i\partial_x, k_y, h_x)\Psi_\beta(x) \,. \tag{B11}$$

Thus we obtain the effective Hamiltonian for edge III as

$$H^{\text{I,edge}}_{iii} = -2\lambda_y k_y s_z - \Delta s_y \tau_y \,. \tag{B12}$$

Therefore, the effective Hamiltonian for the four edges together can be written as

$$H^{\text{I,edge}}_{i} = -2\lambda_y k_y s_z - \Delta s_y \tau_y,$$
$$H^{\text{I,edge}}_{ii} = 2\lambda_x k_x s_z - 2\lambda_x h_x k_x s_y \tau_z - \Delta s_y \tau_y - \frac{h_x}{T} s_x \tau_z,$$
$$H^{\text{I,edge}}_{iii} = -2\lambda_y k_y s_z - \Delta s_y \tau_y,$$
$$H^{\text{I,edge}}_{iv} = 2\lambda_x k_x s_z - 2\lambda_x h_x k_x s_y \tau_z - \Delta s_y \tau_y - \frac{h_x}{T} s_x \tau_z \,. \tag{B13}$$

### 2. Driving by $C_4$ and $\mathcal{T}$ breaking mass term $\Lambda$

For this driving protocol also, we continue as before by writing down the low-energy effective Hamiltonian in the high-frequency limit [Eq. (11) in the main text] around the $\Gamma = (0, 0)$ point as

$$H^{\text{II}}_{\text{eff,k}} = \big(m + t_x k_x^2 + t_y k_y^2\big)\Gamma_3 + 2\lambda_x k_x \Gamma_1 + 2\lambda_y k_y \Gamma_2 + \Delta\Gamma_4 + \frac{\Lambda}{2T}\big(-k_x^2 + k_y^2\big)\Gamma_6 + \lambda_x \Lambda k_x \big(-k_x^2 + k_y^2\big)\Gamma_{16} + \lambda_y \Lambda k_y \big(-k_x^2 + k_y^2\big)\Gamma_{26} + \frac{\Lambda}{2}\big(m + t_x k_x^2 + t_y k_y^2\big)\big(-k_x^2 + k_y^2\big)\Gamma_{36} \,. \tag{B14}$$

For edge I, we consider OBCs (PBCs) along $x$ ($y$) direction and, as before, we rewrite $H^{\text{II}}_{\text{eff,k}} = H_I(-i\partial_x) + H_P(-i\partial_x, k_y, \Lambda)$. We replace $k_x \to -i\partial_x$ and neglect the $k_y^2$ term. Thus we obtain

$$H_{\text{I}} = \big(m - t_x \partial_x^2\big)\Gamma_3 - 2i\lambda_x \partial_x \; \Gamma_1 \,,$$
$$H_P = 2\lambda_y k_y \Gamma_2 + \Delta\Gamma_4 + \frac{\Lambda}{2T}\partial_x^2 \; \Gamma_6 - i\lambda_x \Lambda \;\; \partial_x^3 \Gamma_{16} + \lambda_y \Lambda k_y \partial_x^2 \Gamma_{26} + \frac{m\Lambda}{2}\partial_x^2 \Gamma_{36} - \frac{\Lambda t_x}{2}\partial_x^4 \Gamma_{36} \,, \tag{B15}$$

Here, we consider the pairing amplitude $\Delta$ and the amplitude of the mass term $\Lambda$ to be small and treat them as small perturbation [28,38]. Assuming $\Psi$ to be the zero-energy eigenstate

of $H_{\rm I}$ and following the boundary condition $\Psi(0) = \Psi(\infty) = 0$, we obtain

$$\Psi_\alpha = |\mathcal{N}_x|^2 e^{-\mathcal{A}x} \sin \mathcal{B}x \; e^{ik_y y} \Phi_\alpha \; , \tag{B16}$$

where $\mathcal{A} = \frac{\lambda_x}{t_x}$, $\mathcal{B} = \sqrt{|\frac{m}{t_x}| - \mathcal{A}^2}$, $|\mathcal{N}_x|^2 = \frac{4\mathcal{A}(\mathcal{A}^2+\mathcal{B}^2)}{\mathcal{B}^2}$ and $\Phi_\alpha$ is an eight-component spinor satisfying $\sigma_y s_z \tau_z \Phi_\alpha = -\Phi_\alpha$. Our chosen basis reads

$$\begin{aligned}
\Phi_1 &= |\sigma_y = +1\rangle \otimes |s_z = +1\rangle \otimes |\tau_z = -1\rangle \, , \\
\Phi_2 &= |\sigma_y = -1\rangle \otimes |s_z = +1\rangle \otimes |\tau_z = +1\rangle \, , \\
\Phi_3 &= |\sigma_y = -1\rangle \otimes |s_z = -1\rangle \otimes |\tau_z = -1\rangle \, , \\
\Phi_4 &= |\sigma_y = +1\rangle \otimes |s_z = -1\rangle \otimes |\tau_z = +1\rangle \; .
\end{aligned} \tag{B17}$$

The matrix element of $H_P$ in this basis reads

$$H^{\rm II,edge}_{i,\alpha\beta} = \int_0^\infty dx \; \Psi^\dagger_\alpha(x) H_P(-i\partial_x, k_y, \Lambda) \Psi_\beta(x) \, , \tag{B18}$$

Thus we obtain the effective Hamiltonian for edge I as

$$H^{\rm II,edge}_i = -2\lambda_y k_y s_z - \frac{m\lambda_y \Lambda}{t_x} k_y s_x - \Delta s_y \tau_y - \frac{m\Lambda}{2t_x T} s_y \, , \tag{B19}$$

Similarly, for edge III, we obtain the effective Hamiltonian as

$$H^{\rm II,edge}_{iii} = -2\lambda_y k_y s_z - \frac{m\lambda_y \Lambda}{t_x} k_y s_x - \Delta s_y \tau_y - \frac{m\Lambda}{2t_x T} s_y \, . \tag{B20}$$

For edge II, we employ OBCs (PBCs) along $y$ ($x$) direction. One can thus rewrite $H^{\rm II}_{\rm eff,k} = H_{\rm I}(-i\partial_y) + H_P(-i\partial_y, k_x, \Lambda)$, neglecting the $k_x^2$ term, which yields

$$\begin{aligned}
H_{\rm I} &= \left(m - t_y \partial_y^2\right)\Gamma_3 - 2i\lambda_y \partial_y \Gamma_2 \, , \\
H_P &= 2\lambda_x k_x \Gamma_1 + \Delta\Gamma_4 - \frac{\Lambda}{2T}\partial_y^2 \Gamma_6 + i\lambda_y \Lambda \partial_y^3 \Gamma_{26} \\
&\quad - \lambda_x \Lambda k_x \partial_y^2 \Gamma_{16} - \frac{m\Lambda}{2}\partial_y^2 \Gamma_{36} + \frac{\Lambda t_x}{2}\partial_x^4 \Gamma_{36} \, ,
\end{aligned} \tag{B21}$$

Assuming $\Psi$ to be the zero-energy eigenstate of $H_I$, following the boundary condition $\Psi(0) = \Psi(\infty) = 0$, we obtain

$$\Psi_\alpha = |\mathcal{N}_y|^2 e^{-\tilde{\mathcal{A}}y} \sin \tilde{\mathcal{B}}y \; e^{ik_x x} \chi_\alpha \, , \tag{B22}$$

where $\tilde{\mathcal{A}} = \frac{\lambda_y}{t_y}$, $\tilde{\mathcal{B}} = \sqrt{|\frac{m}{t_y}| - \tilde{\mathcal{A}}^2}$, $|\mathcal{N}_y|^2 = \frac{4\tilde{\mathcal{A}}(\tilde{\mathcal{A}}^2+\tilde{\mathcal{B}}^2)}{\tilde{\mathcal{B}}^2}$ and $\chi_\alpha$ is an eight-component spinor satisfying $\sigma_x \chi_\alpha = \chi_\alpha$. We choose the following basis:

$$\begin{aligned}
\chi_1 &= |\sigma_x = +1\rangle \otimes |s_z = +1\rangle \otimes |\tau_z = -1\rangle \, , \\
\chi_2 &= |\sigma_x = +1\rangle \otimes |s_z = +1\rangle \otimes |\tau_z = +1\rangle \, , \\
\chi_3 &= |\sigma_x = +1\rangle \otimes |s_z = -1\rangle \otimes |\tau_z = -1\rangle \, , \\
\chi_4 &= |\sigma_x = +1\rangle \otimes |s_z = -1\rangle \otimes |\tau_z = +1\rangle \; .
\end{aligned} \tag{B23}$$

The matrix element of $H_P$ in this basis can be written as

$$H^{\rm II,edge}_{ii,\alpha\beta} = \int_0^\infty dy \; \Psi^\dagger_\alpha(y) H_P(-i\partial_y, k_x, \Lambda) \Psi_\beta(y) \, , \tag{B24}$$

We obtain the effective Hamiltonian for edge II as

$$H^{\rm II,edge}_{ii} = 2\lambda_x k_x s_z - \frac{m\lambda_x \Lambda}{t_y} k_x s_x - \Delta s_y \tau_y + \frac{m\Lambda}{2t_y T} s_y \tag{B25}$$

Similarly, for edge IV, we obtain the effective Hamiltonian as

$$H^{\rm II,edge}_{iv} = 2\lambda_x k_x s_z - \frac{m\lambda_x \Lambda}{t_y} k_x s_x - \Delta s_y \tau_y + \frac{m\Lambda}{2t_y T} s_y \; . \tag{B26}$$

Therefore, the effective Hamiltonian for the four edges can be written as

$$\begin{aligned}
H^{\rm II,edge}_i &= -2\lambda_y k_y s_z - \frac{m\lambda_y \Lambda}{t_x} k_y s_x - \Delta s_y \tau_y - \frac{m\Lambda}{2t_x T} s_y, \\
H^{\rm II,edge}_{ii} &= 2\lambda_x k_x s_z - \frac{m\lambda_x \Lambda}{t_y} k_x s_x - \Delta s_y \tau_y + \frac{m\Lambda}{2t_y T} s_y, \\
H^{\rm II,edge}_{iii} &= -2\lambda_y k_y s_z - \frac{m\lambda_y \Lambda}{t_x} k_y s_x - \Delta s_y \tau_y - \frac{m\Lambda}{2t_x T} s_y, \\
H^{\rm II,edge}_{iv} &= 2\lambda_x k_x s_z - \frac{m\lambda_x \Lambda}{t_y} k_x s_x - \Delta s_y \tau_y + \frac{m\Lambda}{2t_y T} s_y \; .
\end{aligned} \tag{B27}$$

## APPENDIX C: MAJORANA CORNER MODE SOLUTIONS

Here, we provide the solutions for the zero-energy MCMs for both the driving protocols.

### 1. Driving by in-plane magnetic field $h_x$

To obtain the corner state solution (when $h_x > \Delta T$), in the intersection between edges I and II, we solve the corresponding edge Hamiltonian for the zero-energy solution. At edge I, we assume a solution of the form

$$\Psi_C \sim e^{-\lambda y} \Phi_C \, , \tag{C1}$$

where $\Phi_C$ is a four component spinor. The secular equation for $\Psi_C$ is given by

$$\det\left[H^{\rm I,edge}_i\right] = 0 \, . \tag{C2}$$

We find four solutions for $\lambda$ as

$$\lambda = \left\{ -\frac{\Delta}{2\lambda_y}, -\frac{\Delta}{2\lambda_y}, \frac{\Delta}{2\lambda_y}, \frac{\Delta}{2\lambda_y} \right\} . \tag{C3}$$

As $\Psi_C$ must vanish at $y \to \infty$, therefore, we obtain two linearly independent solutions, $\Phi^1_C = \{1, 1, -i, i\}^T$ and $\Phi^2_C = \{1, -1, i, i\}^T$. Thus, $\Psi_C$ can be expanded as

$$\Psi_C \sim \alpha \; e^{-\frac{\Delta}{2\lambda_y} y} \Phi^1_C \; + \; \beta \; e^{-\frac{\Delta}{2\lambda_y} y} \Phi^2_C \, . \tag{C4}$$

Similarly, at edge II, we obtain

$$\Psi_C \sim \alpha' \; e^{-\frac{|h_x - \Delta T|}{2\lambda_x T} x} \Phi^3_C \; + \; \beta' \; e^{-\frac{|h_x + \Delta T|}{2\lambda_x T} x} \Phi^4_C \, , \tag{C5}$$

where $\Phi^3_C = \{1, -1, i, i\}^T$ and $\Phi^4_C = \{1, 1, i, -i\}^T$. Considering the wave function $\Psi_C$ to be continuous at the boundary i.e., at $x = y = 0$, we obtain $\alpha = \beta' = 0$ and $\alpha' = \beta$. Hence, the wave function for the Majorana corner mode becomes

$$\begin{aligned}
\Psi_C &\sim \; e^{-\frac{\Delta}{2\lambda_y} y} \Phi^2_C \quad : \text{edgeI} \, , \\
\Psi_C &\sim \; e^{-\frac{|h_x - \Delta T|}{2\lambda_x T} x} \Phi^2_C \, : \text{edgeII} \, ,
\end{aligned} \tag{C6}$$

with localization length $[\frac{|h_x - \Delta T|}{2\lambda_x T}]^{-1}$ and $[\frac{\Delta}{2\lambda_y}]^{-1}$ along $x$ and $y$ directions, respectively. Similarly, one can obtain the remaining zero-energy corner mode solutions.

### 2. Driving by $C_4$ and $\mathcal{T}$ breaking mass term $\Lambda$

#### *a. Weak phase*

In this higher-order phase, $|\frac{m\Lambda}{2t_xT}|, |\frac{m\Lambda}{2t_yT}| > \Delta$. We proceed as before and obtain the following solutions at edges I and II:

$$\Psi_C \sim \alpha\, e^{-\frac{M_{\rm I}-\Delta}{2\lambda_y}y}\Phi_C^1 + \beta\, e^{-\frac{M_{\rm I}+\Delta}{2\lambda_y}y}\Phi_C^2 \quad : \text{edgeI}\,,$$
$$\Psi_C \sim \alpha'\, e^{-\frac{M_{\rm II}+\Delta}{2\lambda_x}x}\Phi_C^3 + \beta'\, e^{-\frac{M_{\rm II}-\Delta}{2\lambda_x}x}\Phi_C^4 : \text{edgeII}\,, \quad \text{(C7)}$$

with $M_{\rm I} = |\frac{m\Lambda}{2t_xT}|$, $M_{\rm II} = |\frac{m\Lambda}{2t_yT}|$ and $\Phi_C^1 = \{1, -i, 1, -i\}^T$, $\Phi_C^2 = \{1, i, 1, i\}^T$, $\Phi_C^3 = \{1, -i, 1, -i\}^T$ and $\Phi_C^4 = \{1, i, 1, i\}^T$. Upon matching the wave function at the boundary ($x = y = 0$), we obtain $\alpha = \alpha'$ and $\beta = \beta'$. Hence, the final form of the zero-energy solutions for the corner mode wave function reads

$$\Psi_C \sim \alpha e^{-\frac{M_{\rm I}-\Delta}{2\lambda_y}y}\Phi_C^1 + \beta e^{-\frac{M_{\rm I}+\Delta}{2\lambda_y}y}\Phi_C^2 \quad : \text{edgeI}\,,$$
$$\Psi_C \sim \alpha e^{-\frac{M_{\rm II}+\Delta}{2\lambda_x}x}\Phi_C^1 + \beta e^{-\frac{M_{\rm II}-\Delta}{2\lambda_x}x}\Phi_C^2 : \text{edgeII}\,. \quad \text{(C8)}$$

Thus, here two corner mode solutions exist for individual edges.

#### *b. Strong phase*

In this phase, we choose $M_{\rm I} < \Delta < M_{\rm II}$. We obtain the following solutions at edges I and II:

$$\Psi_C \sim \alpha\, e^{-\frac{M_{\rm I}+\Delta}{2\lambda_y}y}\Phi_C^1 + \beta\, e^{-\frac{\Delta-M_{\rm I}}{2\lambda_y}y}\Phi_C^2 \quad : \text{edgeI}\,,$$
$$\Psi_C \sim \alpha'\, e^{-\frac{M_{\rm II}-\Delta}{2\lambda_x}x}\Phi_C^3 + \beta'\, e^{-\frac{M_{\rm II}+\Delta}{2\lambda_x}x}\Phi_C^4 : \text{edgeII}\,, \quad \text{(C9)}$$

with $\Phi_C^1 = \{1, i, 1, i\}^T$, $\Phi_C^2 = \{1, -i, -1, i\}^T$, $\Phi_C^3 = \{1, i, 1, i\}^T$, and $\Phi_C^4 = \{1, -i, 1, -i\}^T$. Therefore, matching the wave function at the boundary, we obtain $\alpha = \alpha'$ and $\beta = \beta' = 0$. Hence, the final form of the solutions for the corner-mode wave function becomes

$$\Psi_C \sim e^{-\frac{M_{\rm I}+\Delta}{2\lambda_y}y}\Phi_C^1 \quad : \text{edgeI}\,,$$
$$\Psi_C \sim e^{-\frac{M_{\rm II}-\Delta}{2\lambda_x}x}\Phi_C^1 \quad : \text{edgeII}\,. \quad \text{(C10)}$$

In a similar fashion, one can obtain the zero-energy solutions for the remaining MCMs in both these phases.


[1] A. Y. Kitaev, Phys. Usp. **44**, 131 (2001).
[2] X.-L. Qi and S.-C. Zhang, Rev. Mod. Phys. **83**, 1057 (2011).
[3] M. Z. Hasan and C. L. Kane, Rev. Mod. Phys. **82**, 3045 (2010).
[4] C. Nayak, S. H. Simon, A. Stern, M. Freedman, and S. Das Sarma, Rev. Mod. Phys. **80**, 1083 (2008).
[5] A. Das, Y. Ronen, Y. Most, Y. Oreg, M. Heiblum, and H. Shtrikman, Nat. Phys. **8**, 887 (2012).
[6] M. T. Deng, S. Vaitiekenas, E. B. Hansen, J. Danon, M. Leijnse, K. Flensberg, J. Nygård, P. Krogstrup, and C. M. Marcus, Science **354**, 1557 (2016).
[7] L. Fu and C. L. Kane, Phys. Rev. Lett. **100**, 096407 (2008).
[8] J. D. Sau, R. M. Lutchyn, S. Tewari, and S. Das Sarma, Phys. Rev. Lett. **104**, 040502 (2010).
[9] R. M. Lutchyn, J. D. Sau, and S. Das Sarma, Phys. Rev. Lett. **105**, 077001 (2010).
[10] X.-L. Qi, T. L. Hughes, and S.-C. Zhang, Phys. Rev. B **82**, 184516 (2010).
[11] Y. Oreg, G. Refael, and F. von Oppen, Phys. Rev. Lett. **105**, 177002 (2010).
[12] V. Mourik, K. Zuo, S. M. Frolov, S. R. Plissard, E. P. A. M. Bakkers, and L. P. Kouwenhoven, Science **336**, 1003 (2012).
[13] P. Zareapour, A. Hayat, S. Y. F. Zhao, M. Kreshchuk, A. Jain, D. C. Kwok, N. Lee, S.-W. Cheong, Z. Xu, A. Yang, *et al.*, Nat. Commun. **3**, 1056 (2012).
[14] A. D. K. Finck, D. J. Van Harlingen, P. K. Mohseni, K. Jung, and X. Li, Phys. Rev. Lett. **110**, 126406 (2013).
[15] Q. L. He, L. Pan, A. L. Stern, E. C. Burks, X. Che, G. Yin, J. Wang, B. Lian, Q. Zhou, E. S. Choi, K. Murata, X. Kou, Z. Chen, T. Nie, Q. Shao, Y. Fan, S.-C. Zhang, K. Liu, J. Xia, and K. L. Wang, Science **357**, 294 (2017).
[16] Q. Liu, C. Chen, T. Zhang, R. Peng, Y.-J. Yan, Chen-Hao-Ping Wen, X. Lou, Y.-L. Huang, J.-P. Tian, X.-L. Dong, G.-W. Wang, W.-C. Bao, Q.-H. Wang, Z.-P. Yin, Z.-X. Zhao, and D.-L. Feng, Phys. Rev. X **8**, 041056 (2018).
[17] R.-J. Slager, L. Rademaker, J. Zaanen, and L. Balents, Phys. Rev. B **92**, 085126 (2015).
[18] W. A. Benalcazar, B. A. Bernevig, and T. L. Hughes, Science **357**, 61 (2017).
[19] W. A. Benalcazar, B. A. Bernevig, and T. L. Hughes, Phys. Rev. B **96**, 245115 (2017).
[20] Z. Song, Z. Fang, and C. Fang, Phys. Rev. Lett. **119**, 246402 (2017).
[21] J. Langbehn, Y. Peng, L. Trifunovic, F. von Oppen, and P. W. Brouwer, Phys. Rev. Lett. **119**, 246401 (2017).
[22] F. Schindler, A. M. Cook, M. G. Vergniory, Z. Wang, S. S. Parkin, B. A. Bernevig, and T. Neupert, Science adv. **4**, eaat0346 (2018).
[23] E. Khalaf, Phys. Rev. B **97**, 205136 (2018).
[24] M. Geier, L. Trifunovic, M. Hoskam, and P. W. Brouwer, Phys. Rev. B **97**, 205135 (2018).
[25] S. Franca, J. van den Brink, and I. C. Fulga, Phys. Rev. B **98**, 201114(R) (2018).
[26] X. Zhu, Phys. Rev. B **97**, 205134 (2018).
[27] T. Liu, J. J. He, and F. Nori, Phys. Rev. B **98**, 245413 (2018).
[28] Z. Yan, F. Song, and Z. Wang, Phys. Rev. Lett. **121**, 096803 (2018).
[29] Z. Wang, B. J. Wieder, J. Li, B. Yan, and B. A. Bernevig, Phys. Rev. Lett. **123**, 186401 (2019).
[30] Y. Wang, M. Lin, and T. L. Hughes, Phys. Rev. B **98**, 165144 (2018).
[31] M. Ezawa, Phys. Rev. Lett. **120**, 026801 (2018).
[32] M. Ezawa, Sci. Rep. **9**, 5286 (2019).
[33] D. Călugăru, V. Juričić, and B. Roy, Phys. Rev. B **99**, 041301(R) (2019).
[34] R. W. Bomantara, L. Zhou, J. Pan, and J. Gong, Phys. Rev. B **99**, 045441 (2019).
[35] L. Trifunovic and P. W. Brouwer, Phys. Rev. X **9**, 011012 (2019).
[36] R.-X. Zhang, W. S. Cole, and S. Das Sarma, Phys. Rev. Lett. **122**, 187001 (2019).
[37] Y. Volpez, D. Loss, and J. Klinovaja, Phys. Rev. Lett. **122**, 126402 (2019).

[38] Z. Yan, Phys. Rev. B **100**, 205406 (2019).
[39] Y.-J. Wu, J. Hou, Y.-M. Li, X.-W. Luo, X. Shi, and C. Zhang, Phys. Rev. Lett. **124**, 227001 (2020).
[40] S. J. De, U. Khanna, and S. Rao, Phys. Rev. B **101**, 125429 (2020).
[41] K. Laubscher, D. Chughtai, D. Loss, and J. Klinovaja, Phys. Rev. B **102**, 195401 (2020).
[42] B. Roy, Phys. Rev. B **101**, 220506(R) (2020).
[43] S.-B. Zhang and B. Trauzettel, Phys. Rev. Res. **2**, 012018(R) (2020).
[44] S.-B. Zhang, A. Calzona, and B. Trauzettel, Phys. Rev. B **102**, 100503(R) (2020).
[45] S.-B. Zhang, W. B. Rui, A. Calzona, S.-J. Choi, A. P. Schnyder, and B. Trauzettel, Phys. Rev. Res. **2**, 043025 (2020).
[46] Sayed Ali Akbar Ghorashi, T. L. Hughes, and E. Rossi, Phys. Rev. Lett. **125**, 037001 (2020).
[47] S. A. A. Ghorashi, X. Hu, T. L. Hughes, and E. Rossi, Phys. Rev. B **100**, 020509(R) (2019).
[48] C. Zeng, T. D. Stanescu, C. Zhang, V. W. Scarola, and S. Tewari, Phys. Rev. Lett. **123**, 060402 (2019).
[49] H. Xue, Y. Yang, F. Gao, Y. Chong, and B. Zhang, Nat. Mater. **18**, 108 (2019).
[50] X.-D. Chen, W.-M. Deng, F.-L. Shi, F.-L. Zhao, M. Chen, and J.-W. Dong, Phys. Rev. Lett. **122**, 233902 (2019).
[51] B.-Y. Xie, G.-X. Su, H.-F. Wang, H. Su, X.-P. Shen, P. Zhan, M.-H. Lu, Z.-L. Wang, and Y.-F. Chen, Phys. Rev. Lett. **122**, 233903 (2019).
[52] S. Imhof, C. Berger, F. Bayer, J. Brehm, L. W. Molenkamp, T. Kiessling, F. Schindler, C. H. Lee, M. Greiter, T. Neupert, and R. Thomale, Nat. Phys. **14**, 925 (2018).
[53] N. H. Lindner, G. Refael, and V. Galitski, Nat. Phys. **7**, 490 (2011).
[54] B. Dóra, J. Cayssol, F. Simon, and R. Moessner, Phys. Rev. Lett. **108**, 056602 (2012).
[55] M. S. Rudner, N. H. Lindner, E. Berg, and M. Levin, Phys. Rev. X **3**, 031005 (2013).
[56] M. Thakurathi, A. A. Patel, D. Sen, and A. Dutta, Phys. Rev. B **88**, 155133 (2013).
[57] M. C. Rechtsman, J. M. Zeuner, Y. Plotnik, Y. Lumer, D. Podolsky, F. Dreisow, S. Nolte, M. Segev, and A. Szameit, Nature **496**, 196 (2013).
[58] L. J. Maczewsky, J. M. Zeuner, S. Nolte, and A. Szameit, Nat. Commun. **8**, 13756 (2017).
[59] A. Eckardt, Rev. Mod. Phys. **89**, 011004 (2017).
[60] J. H. Shirley, Phys. Rev. **138**, B979 (1965).
[61] F. Grossmann, T. Dittrich, P. Jung, and P. Hänggi, Phys. Rev. Lett. **67**, 516 (1991).
[62] T. Oka and S. Kitamura, Annu. Rev. Condens. Matter Phys. **10**, 387 (2019).
[63] M. Benito, A. Gómez-León, V. M. Bastidas, T. Brandes, and G. Platero, Phys. Rev. B **90**, 205127 (2014).
[64] T. Nag, V. Juričić, and B. Roy, Phys. Rev. Res. **1**, 032045(R) (2019).
[65] Y. Peng and G. Refael, Phys. Rev. Lett. **123**, 016806 (2019).
[66] R. Seshadri, A. Dutta, and D. Sen, Phys. Rev. B **100**, 115403 (2019).
[67] S. Chaudhary, A. Haim, Y. Peng, and G. Refael, Phys. Rev. Res. **2**, 043431 (2020).
[68] M. Rodriguez-Vega, A. Kumar, and B. Seradjeh, Phys. Rev. B **100**, 085138 (2019).
[69] A. K. Ghosh, G. C. Paul, and A. Saha, Phys. Rev. B **101**, 235403 (2020).
[70] B. Huang and W. V. Liu, Phys. Rev. Lett. **124**, 216601 (2020).
[71] H. Hu, B. Huang, E. Zhao, and W. V. Liu, Phys. Rev. Lett. **124**, 057001 (2020).
[72] R. W. Bomantara and J. Gong, Phys. Rev. B **101**, 085401 (2020).
[73] K. Plekhanov, M. Thakurathi, D. Loss, and J. Klinovaja, Phys. Rev. Res. **1**, 032013(R) (2019).
[74] R. X. Zhang and Z. C. Yang, arXiv:2005.08970.
[75] A. Tiwari, A. Jahin, and Y. Wang, arXiv:2005.12291.
[76] Y. Peng, Phys. Rev. Res. **2**, 013124 (2020).
[77] T. Nag, V. Juričić, and B. Roy, arXiv:2009.10719.
[78] R. Jackiw and C. Rebbi, Phys. Rev. D **13**, 3398 (1976).
[79] L. Fu and C. L. Kane, Phys. Rev. B **76**, 045302 (2007).
[80] B. A. Bernevig, T. L. Hughes, and S.-C. Zhang, Science **314**, 1757 (2006).
[81] M. König, S. Wiedmann, C. Brüne, A. Roth, H. Buhmann, L. W. Molenkamp, X.-L. Qi, and S.-C. Zhang, Science **318**, 766 (2007).
[82] D. Hsieh, D. Qian, L. Wray, Y. Xia, Y. S. Hor, R. J. Cava, and M. Z. Hasan, Nature **452**, 970 (2008).
[83] S. Hart, H. Ren, T. Wagner, P. Leubner, M. Mühlbauer, C. Brüne, H. Buhmann, L. W. Molenkamp, and A. Yacoby, Nat. Phys. **10**, 638 (2014).
[84] F. Lüpke, D. Waters, S. C. de la Barrera, M. Widom, D. G. Mandrus, J. Yan, R. M. Feenstra, and B. M. Hunt, Nat. Phys. **16**, 526 (2020).
[85] Y. H. Wang, H. Steinberg, P. Jarillo-Herrero, and N. Gedik, Science **342**, 453 (2013).
[86] Y.-G. Peng, C.-Z. Qin, D. Zhao, Y. X. Shen, X.-Y. Xu, M. Bao, H. Jia, and X.-F. Zhu, Nat. Commun. **7**, 13368 (2016).
[87] S. Nadj-Perge, I. K. Drozdov, J. Li, H. Chen, S. Jeon, J. Seo, A. H. MacDonald, B. Andrei Bernevig, and A. Yazdani, Science **346**, 602 (2014).
[88] N. Goldman and J. Dalibard, Phys. Rev. X **4**, 031027 (2014).
[89] J. Struck, J. Simonet, and K. Sengstock, Phys. Rev. A **90**, 031601(R) (2014).
[90] P. Wang, Z.-Q. Yu, Z. Fu, J. Miao, L. Huang, S. Chai, H. Zhai, and J. Zhang, Phys. Rev. Lett. **109**, 095301 (2012).
[91] X. Zhou, X.-W. Luo, G. Chen, S. Jia, and C. Zhang, Phys. Rev. A **100**, 063630 (2019).
[92] B.-Z. Wang, Y.-H. Lu, W. Sun, S. Chen, Y. Deng, and X.-J. Liu, Phys. Rev. A **97**, 011605(R) (2018).
[93] Y.-J. Lin, K. Jiménez-García, and I. B. Spielman, Nature **471**, 83 (2011).
[94] L. Huang, Z. Meng, P. Wang, P. Peng, S.-L. Zhang, L. Chen, D. Li, Q. Zhou, and J. Zhang, Nat. Phys. **12**, 540 (2016).
[95] Z. Meng, L. Huang, P. Peng, D. Li, L. Chen, Y. Xu, C. Zhang, P. Wang, and J. Zhang, Phys. Rev. Lett. **117**, 235304 (2016).
[96] W. Sun, B.-Z. Wang, X.-T. Xu, C.-R. Yi, L. Zhang, Z. Wu, Y. Deng, X.-J. Liu, S. Chen, and J.-W. Pan, Phys. Rev. Lett. **121**, 150401 (2018).
[97] W. Deng, X. Huang, J. Lu, V. Peri, F. Li, S. D. Huber, and Z. Liu, Nat. Commun. **11**, 3227 (2020).
[98] M. Lejman, G. Vaudel, I. C. Infante, P. Gemeiner, V. E. Gusev, B. Dkhil, and P. Ruello, Nat. Commun. **5**, 4301 (2014).
[99] Y. Ding, Y. Peng, Y. Zhu, X. Fan, J. Yang, B. Liang, X. Zhu, X. Wan, and J. Cheng, Phys. Rev. Lett. **122**, 014302 (2019).